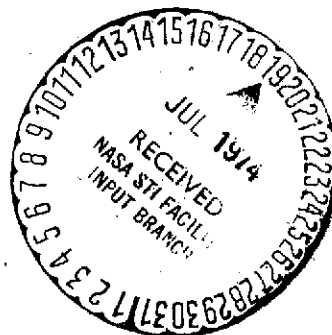


CONING MOTION, AUTOROTATION AND VORTEX SYSTEMS  
OF SLENDER MISSILES

M. Fiechter

Translation of "Kegelpendelung, Autorotation  
und Wirbelsysteme schlanker Flugkörper".  
Zeitschrift für Flugwissenschaften 20, No. 8,  
1972, pp. 281-292.



(NASA-TT-F-15705) CONING MOTION,  
AUTOROTATION AND VORTEX SYSTEMS OF  
SLENDER MISSILES (Scientific Translation  
Service) 37 p HC \$5.00 CSCL 16E  
35

N74-28348

G3/31 43160  
Unclas

NATIONAL AERONAUTICS AND SPACE ADMINISTRATION  
WASHINGTON, D. C. 20546 JUNE 1974

1. Report No. NASA TT F-15,705	2. Government Accession No.	3. Recipient's Catalog No.	
4. Title and Subtitle CONING MOTION, AUTOROTATION AND VORTEX SYSTEMS OF SLENDER MISSILES		5. Report Date June, 1974	
		6. Performing Organization Code	
7. Author(s) M. Fiechter		8. Performing Organization Report No.	
		10. Work Unit No.	
9. Performing Organization Name and Address SCITRAN Box 5456 Santa Barbara, CA 93108		11. Contract or Grant No. NASW-2483	
		13. Type of Report and Period Covered Translation	
12. Sponsoring Agency Name and Address National Aeronautics and Space Administration Washington, D.C. 20546		14. Sponsoring Agency Code	
15. Supplementary Notes  Translation of "Kegelpendelung, Autorotation und Wirbelsysteme schlanker Flugkörper". Zeitschrift für Flugwissenschaften 20, No. 8, 1972, pp. 281-292.			
16. Abstract The coning motion of missiles for a slenderness between 15 and 20.5 was tested in the subsonic wind tunnel of the ISL at a speed of 34.2 m/sec and a Reynolds number (with respect to body diameter D) of 110,000. The conical pendulum motion of the projectile was investigated, and it was found that the autorotation could be attributed to the shedding of body vortices. The coning motion could be prevented by disturbing the body boundary layer in an asymmetric way.			
17. Key Words (Selected by Author(s))		18. Distribution Statement  Unclassified - Unlimited	
19. Security Classif. (of this report) Unclassified	20. Security Classif. (of this page) Unclassified	21. No. of Pages 35	22. Price 5.00

# CONING MOTION, AUTOROTATION AND VORTEX SYSTEMS OF SLENDER MISSILES \*

M. Fiechter \*\*

## 1. INTRODUCTION

/281\*\*\*

Flight trajectory measurements and wind tunnel investigations [1-4] showed that conical pendulum motion of fin-stabilized, very slender projectiles cannot be described using conventional flight mechanical models, such as the coupling of roll and conical pendulum motion frequencies. If sufficient stabilizing pitch moments are provided by sufficiently large stabilization fins, it is possible for the coning angles to increase to up to  $10^\circ$  because of large perturbation moments. If even larger coning angles are excited, catastrophic yaw can occur. The associated yaw moments push the body longitudinal axis around the surface of a cone around the flight trajectory tangent. Coning motion is a term which has been adapted for this type of flight motion. There is apparently also a connection between the yaw moments and the asymmetric body vortices.

---

\* Expanded text of a lecture at the 6th Working Group Session "Aerodynamic Properties of Slender Projectiles" on November 15, 1968 in Goettingen. The author wishes to thank Mr. R. Ramshorn and Dr. E. David for suggestions, Mr. Risser and Mr. A. Schaub for test installations, measurements and evaluations as well as Dr. H. Oertel for critical review of the manuscript.

\*\* German-French Research Institute, St. Louis, France (ISL)

\*\*\* Numbers in the margin indicate pagination of original foreign text.

The flow processes during coning motion have up to the present not been investigated sufficiently. This is why model tests were carried out in the subsonic wind tunnel of the ISL. In order to avoid the roll-coning motion coupling, the shoulder angle of the stabilization fins was selected according to [5] so that the roll moments vanish at angles of attack  $<15^\circ$ . In this way it becomes possible to investigate the aerodynamic processes which are only related to the coning motion at large coning angles.

The beginning of the final state of coning motion could be detected from the behavior of the vortices which are shed asymmetrically by the body. In addition it was possible to establish a relationship between vortex shedding and autorotation or the directional change of the roll moments. This was also done in [6].

Finally it was possible to develop a method with which it is possible to avoid coning motion.

## 2. NOTATION

### 2.1. Aerodynamic variables

$C_l$	Roll moment coefficient $(= M_x/q S D)$
$C_m$	Pitch moment coefficient $(= M_y/q S D)$
$C_n$	Yaw moment coefficient $(= M_z/q S D)$
$C_x$	Tangential force coefficient $(= X/q S)$
$C_y$	Side force coefficient $(= Y/q S)$
$C_z$	Normal force coefficient $(= Z/q S)$
$M_x$	Roll moment
$M_y$	Pitch moment
$M_z$	Yaw moment

/282

$n_y$	Side force per unit length
$q$	Stagnation pressure of undisturbed flow [ $= (\rho/2) V^2$ ]
$Re$	Reynolds number ( $= \rho V D / \mu$ )
$V$	Velocity of undisturbed flow
$X, Y, Z$	Tangential, side and normal forces
$\mu$	Viscosity
$\nu$	Kinematic viscosity
$\rho$	Density

## 2.2. Geometric variables

$D$	Diameter of cylindrical body, reference length
$G$	Center of gravity, moment reference point
$L$	Total model length
$R$	Body radius
$r$	Radial distance between body longitudinal axis and trajectory tangent (Figure 12)
$r_{W_i}$	Radial distance between vortex axes and body longitudinal axes
$S$	Cross section area of body, reference area ( $= \pi D^2/4$ )
$x, y, z$	Coordinates in body fixed system, reference point: body tip
$x_0$	x-Coordinate, reference point: center of gravity
$x_G$	Distance between moment reference point $G$ and tail
$\alpha$	Angle of attack
$\gamma$	Inclination angle of disturbing elements
$\eta$	Adjustment angle of fins with respect to body axis
$\vartheta$	Coning angle
$\varphi$	Circumference angle, roll angle: $\varphi = 0$ in the angle of attack plane along the incident flow side.

### 2.3. Flight mechanical quantities

J	Transverse moment of inertia
$M_F$	Centrifugal force moment according to Equation (8)
$n_P$	Coning frequency in rps
$n_R$	Rotation frequency in rps
$\omega_P$	Circular frequency of coning motion ( $= 2\pi n_P$ )
$\omega_R$	Circular frequency of rotation ( $= 2\pi n_R$ )

The stationary flow processes are referred to the angle of attack  $\alpha$  and the flow processes during coning motion are referred to the coning angle  $\vartheta$ . In order to compare both processes, the body fixed reference system  $x, y, z$  was selected according to Figure 1. For the flow processes,  $x = 0$  at the body tip. For coning motion,  $x_0 = 0$  at the body center of gravity G. The reference plane is the angle of attack plane as well as the coning motion plane. Both are specified by the wind tunnel axis and the body longitudinal axis. During coning motion, the coning plane also rotates around the wind tunnel axis at the coning frequency  $n_P$ .

### 3. TEST INSTALLATIONS, MODELS AND MEASUREMENT TECHNIQUES

The tests were carried out in the subsonic wind tunnel of the ISL, a circulation wind tunnel with an open test section of 1.2 m nozzle diameter. The flow velocity is  $V = 34.2$  m/sec. The model used in most cases had a cylindrical body with a diameter of  $D = 5$  cm, a 3 D ogive tip with the AGARD-B profile and a total length of  $L = 15.54 D$  (Figure 2). The cylindrical part of the body could be extended up to  $L = 20.5 D$  (Table 1). Four Delta fins with a  $25^\circ$  shoulder angle ( $= 65^\circ$  sweepback angle) were installed at the body tail. They had an overall span of

3 D and were arranged in the form of a cross. They could be adjusted at  $\eta = 2^\circ$  and  $4^\circ$  with respect to the body longitudinal axis.

Balances with strain gauges were installed in the model for measuring forces and moments. They were recorded on pen recorders or oscillographs. Pressure measurement taps were used for measuring pressure over the surface of the body. The vortex field along the wake side of the body was measured using a hemispherical probe with a diameter of 3.5 mm.

#### 4. STATIC MEASUREMENTS

##### 4.1. Body of revolution without fins

##### 4.1.1. Symmetric vortex pair

In [7] it was stated that a vortex pair produced over bodies of revolution along the wake side at angles of attack of  $\alpha > 5^\circ$ .

/ 50

TABLE 1\*

Model No.	D	L/D	$x_G/L$	$J$	$M_H$	$\vartheta_E$	$n_p$
	[cm]			[m <sup>2</sup> kg]	[N m]	[°]	[U/sec]
1	5	15,54	0,48	0,0856	1,90	30	1,13
2	5	15,54	0,48	0,3009	1,83	27	0,59
3	3	15,0	0,50	0,0078	0,41	30	1,68
4	5	20,5	0,50	0,1858	1,61	17,5	0,84
5	5	18,8	0,68	0,2369	4,07	22	1,07
6	5	18,1	0,73	0,1160	0,56	20	0,63
7	5	15,0	0,50	0,0899	1,70	30	1,01

\* Translator's note: Commas in numbers represent decimal points.

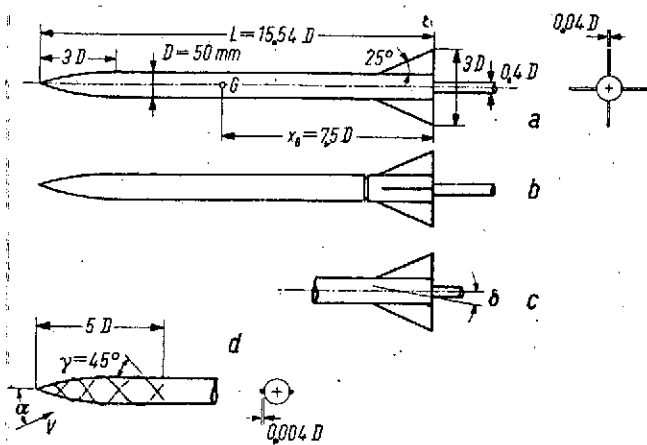


Figure 2. Wind tunnel models.

a- fins not at incidence;  
b- tail with rotatable fins;  
c- all four fins at incidence in  
the same direction; d- two  
perturbation wires attached to  
the surface

Vortex	M = 0,1 (ISL)						M = 1,41 (According to [6])	
	Boundary layer disturbed		Coning motion				$\alpha$ x/D	$\alpha$ [°]
			np = 1 rps		np = 2 rps			
	$\alpha$ x/D	$\alpha$ [°]	$\vartheta$ L/D	$\vartheta$ [°]	$\vartheta$ L/D	$\vartheta$ [°]		
W 1	3,4	14	5,0	19	4,7	18	5,0	19
W 2	4,7	19	6,4	24	5,8	22	6,0	23
W 2, 3	5,8	24	7,8	30	7,1	27		
W 3	6,9	28					7,6	29

It is produced at the body tip and rotates in the direction opposite to the body. It moves along the body at the velocity  $V \cos \alpha$ . Over the cylindrical part of the body, the vortex axes lie along two meridian planes which are symmetric with respect to the angle of attack plane. These planes make an angle of  $[\varphi = 180^\circ \pm 23^\circ]$ . Their radial distance  $r_W$  from the body longitudinal axis increases in the angle of attack range  $[10^\circ < \alpha < 25^\circ]$  according to the product of distance  $x$  from the body tip and the

\*Translator's Note: Commas in numbers represent decimal points.



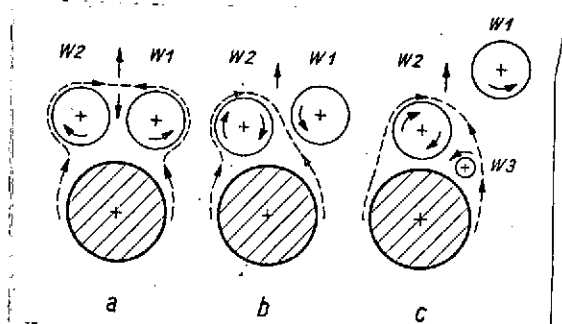


Figure 3. Diagram of vortex shedding.

- - - the surface boundary layer encloses the wake region tied to the body.

a- vortices W1 and W2 shortly before shedding; b- vortex W1 shedded and excluded from the wake region; c- vortex W3 has again formed

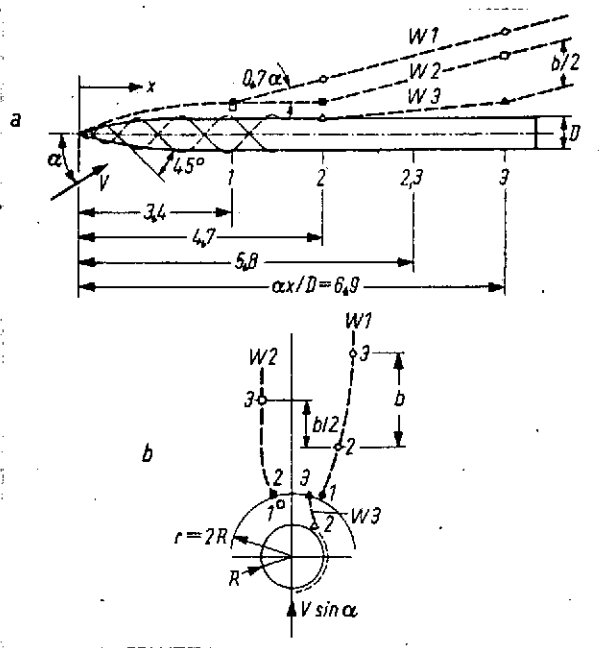


Figure 4. Diagram of vortex shedding.

- - - - boundary layer greatly disturbed;  
— — — axes of vortices W1, W2, W3

angle of attack  $\alpha$ :

$$r_W = 0.12 x \alpha + R \quad (\alpha \text{ in rad})$$

In addition to the radial distance, the diameter of the vortex cores increases approximately with  $0.14 x \alpha$ . The vortex circulation increases according to  $0.14 \pi V x \alpha^2$ . In this connection we would like to refer to the wind tunnel investigations of the vortex system around a body of revolution which were carried out by F. R. Grosche at the AVA Goettingen of the DFVLR [8].

Without vortices, the flow which is divided along the incident direction of the body at incidence, would again run together on the wake side. However, the flow is forced around the vortices. At a circumference angle of  $80^\circ < \varphi < 110^\circ$ , the flow separates from the body. A wake region is produced which forms

a unit with the body and is closed off from the external flow by means of a boundary layer. The outer flow takes boundary layer material from the separation point, drags it into the boundary layer and supplies it to the vortex cores. There the degree of turbulence is about 20 times higher than that of the outer flow. Figure 3 gives a diagram of flow shedding.

In the case where  $r_W \approx 2R = D$  and therefore  $\alpha x/D \approx 4.2$ , the vortices become asymmetric with respect to the angle of attack plane. Their core diameter is increased to  $0.6 D$ . The asymmetric vortices remain approximately at this radial distance, until at  $\alpha x/D \approx 7.3$  one of the two vortices is shedded.

When there are small disturbances in the incident flow or on the body surface, it is possible for the asymmetric vortices to sporadically exchange sides. They then take on a position which is mirror-symmetric with respect to the angle of attack plane. In order to prevent this, the boundary layer of the body was disturbed in a manner which is asymmetric with respect to the angle of attack plane.

#### 4.1.2. Asymmetric shedding of the vortices

Thin wires 0.25 mm in diameter or bands with a cross section of 5 mm x 0.25 mm were used for asymmetric disturbance of the body boundary layer. These were applied to the surfaces of the models with a screw pitch angle of  $\gamma = 45^\circ$ . In Figure 4, on the side facing the observer, the angle between the incident flow direction and these perturbation elements is greater than on the other side. The larger angle corresponds to a greater disturbance in the flow next to the wall. The screw configuration of the perturbation elements was selected in order to conserve the flow asymmetry even when the roll position is changed during pressure measurements and during dynamic measurements.

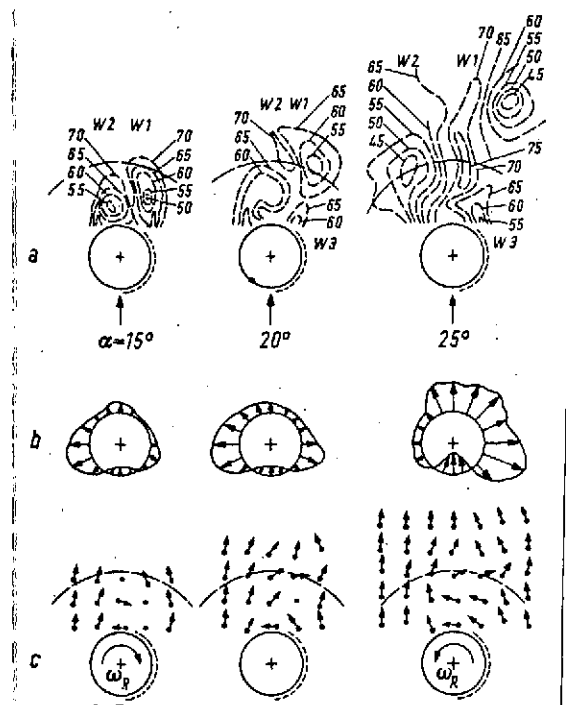


Figure 5. Vortices over body of revolution.

a- Lines of equal stagnation pressure (in mm water column),  $x/D = 12$ ; b- pressure distribution,  $x/D = 12.5$ ; c- Direction distribution  $x/D = 12$ .

- - - boundary layer disturbed more on one side;  
 — — — tip circle of the fins

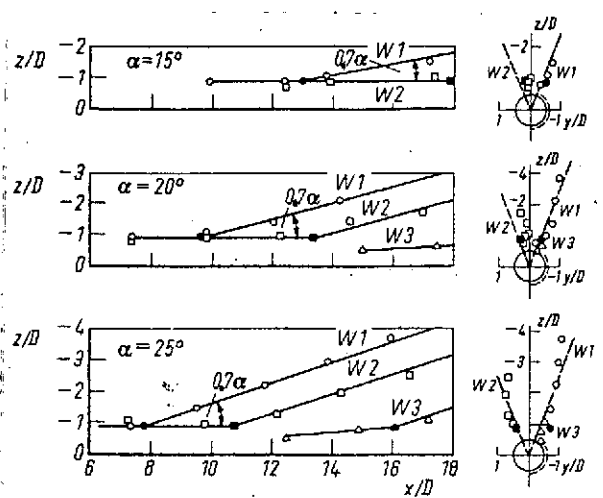


Figure 6. Position of vortex centers.

●	■	▲
W 1	W 2	W 3

- - - boundary layer greatly disturbed; according to [7]  
 — — —  $\varphi = 180^\circ \pm 23^\circ$

In order to describe the shedding process, the pressure and direction measurements were selected in a normal plane for angles of attack of  $15^\circ$ ,  $20^\circ$  and  $25^\circ$  in Figure 5. For the angle of attack  $\alpha = 15^\circ$  the vortices are asymmetric with respect to the angle of attack plane. Because of the greater perturbation of the right side of the body, the right vortex  $W1$  is farther away from the body than the left vortex  $W2$ .  $W1$  with  $x/D \approx 3.4$  has reached the distance  $r_w \approx 2R$ . Since the vortex perturbation becomes asymmetric when it is first introduced for  $\alpha > 5^\circ$ , this

/284

shedding occurs at a much lower  $\alpha x/D$  value than on a body without the perturbation (in that case, asymmetry starts at  $\alpha x/D \approx 4.2$  and the first shedding occurs at  $\alpha x/D \approx 7.3$ ).

Since the external flow always has the tendency to become close again just behind the body, as the vortex distance increases, it penetrates further between the vortex W1 and the body. At  $r_W \approx 2R$ , W1 has more incident flow in the radial direction than in the tangential direction. The boundary layer becomes fanned before it is overtaken by the vortex chord. The rotation of W1 is attenuated more than that of W2. The distance of W1 increases and the outer flow penetrates even more. It is tangent to W1 from the inside, opposing the direction of rotation. This shedding process remains steady. The vortex axis has a bend and W1 is excluded from the wake region.

During the shedding process of W1, the left vortex W2 moves into the free space in the direction of the angle of attack plane. In this way W2 again has more tangential flow than radial flow and therefore remains in the wake region. However, there is the flow from the right to W2 which is opposed to the vortex rotation. This is shown in Figure 5 for  $\alpha = 25^\circ$ . In this way, W2 is braked from the right and is prepared for shedding.

In addition, a new vortex W3 is formed on the right side. When it becomes sufficiently large, it pushes W2 so far to the left that the external flow sheds W2 at  $\alpha x/D \approx 4.7$  from the left. In the same way, the shedding process is repeated with the newly produced vortices W3 and W4 (see also the ISL film "Vortex Systems" and [9]).

From the pressure measurements in the various normal planes and angles of attack, we determined the positions of the vortex centers in Figure 6. It was found that the  $\alpha x/D$  values for the

shedding locations of the vortices were always the same (see also Table 2). In addition, all of the vortex axes leave the wake region at the same angle of  $0.7 \alpha$  with respect to the body longitudinal axis.

#### 4.1.3. Shedding of the vortices and Karman vortex street

The measurement results shown in Figures 5 and 6 can be used to make a comparison between the steady shedding of vortices from the body of revolution at incidence and the unsteady shedding of vortices of circular cylinders which are oblique with respect to the flow. This was also done in [6]. The steady, three-dimensional shedding of vortices W1 and W2 corresponds to the "starting vortices" in circular cylinders in an oblique flow. The shedding of the subsequent vortices of the unsteady separation of vortices which is periodic in time corresponds to the Karman vortex street. /285

Since the vortices move at  $V \cos \alpha$  along the body of revolution at incidence, we find that the time between the shedding rotation of vortex W2 to that of W3 is given by

$$\frac{x_{W3} - x_{W2}}{V \cos \alpha} = \frac{T}{2}, \quad (1)$$

where  $T = 1/n$  is the time separation of the vortex sequence on the same side of the circular cylinder in the oblique flow;  $n$  is the frequency in the vortex street. For example, according to [6] the Strouhal number for the vortex street with Reynolds numbers  $500 < Re < 300,000$  is given by the equation  $(V_Q = \text{incident velocity})$ :

$$St = \frac{nD}{V_Q} = 0.20 \pm 0.02. \quad (2)$$

If the incident velocity is set equal to the normal flow component for the body of revolution at incidence

$$V_Q = V \sin \alpha \approx V \alpha,$$

then from Equations (1) and (2) we find the following distance between the shedding values

$$\frac{\alpha (x_{W_3} - x_{W_2})}{D} = \frac{1}{2 St} = 2.5 \pm 0.25, \quad (3)$$

which corresponds approximately with the measured value of 2.2. We measured about 1/2 this value, or 1.3, for the difference between the first two vortices (Figure 4).

Using the vortex separation given in [6]

$$b = \frac{D}{0.28} = \text{const} \quad (4)$$

in the vortex street and from Equation (3), we find that the angle between the vortex axes after shedding and the body longitudinal axis of the body of revolution at incidence is given by

$$\frac{\alpha St}{0.28} = (0.7 \pm 0.07) \alpha = \text{const}; \quad (5)$$

the measurement gave 0.7  $\alpha$  and is given in Figure 6.]

If we also compare the measurement results in [10] over a circular cylinder which is accelerated in water from rest and if we set  $V_0 t = x$  for the body of revolution at incidence, then the asymmetry of the vortices should start at  $\alpha x/D \approx 4$ . In the wind tunnel we measured 4.2. The first vortex according to [10] is completely separated at  $\alpha x/D = 8.5$  in the water tunnel, whereas under steady conditions in the wind tunnel we measured a smaller value of 7.3.

Even though the vortices are steady in one case for the slender body of revolution at incidence and even though they are shedded three-dimensionally, whereas in the other case they separate in an unsteady way from the circular cylinder in an oblique flow and do not have any velocity in the direction of the vortex axes, we nevertheless find a satisfactory agreement between both experimental findings. A detailed description is given in [6].

#### 4.1.4. Forces and moments

Because of the vortex asymmetry, the pressure distribution according to the examples in Figure 5b becomes asymmetric with respect to the angle of attack plane. The pressure is the lowest along the side having the vortex closest to the body. The integration of the measured pressure distributions over the individual cross sections results in the distribution of the side forces along the  $x$  axis. (Figure 7). According to the values of  $\alpha x/D$ , the side force minimum follows the shedding location of vortex W1 with increasing angle of attack, in the direction of the body tip. The side force changes sign with the shedding location of vortex W2. It exceeds an extreme value and passes through the second zero at the shedding location of W3. As will be shown later on, the yaw moment corresponding to this side force distribution with G as a reference point changes sign at  $\alpha = 21^\circ$ .

Without disturbance of the boundary layer, the side forces and yaw moments can only be found for  $\alpha > 28^\circ$  in Figure 8, at which time the first vortex is shedded at the tail with  $\alpha x/D \approx 7.3$ . /286

When there is boundary layer disturbance, side forces occur at  $\alpha > 5^\circ$ , as soon as vortices have formed. When the vortex W2 is shedded, the yaw moment has a maximum value and changes sign halfway between the shedding values W2 and W3. This value is called  $\alpha x/D_{W2.3}$ . It is shown in Figures 4 and Table 2. The side forces (Figure 8a) reach a maximum value when shedding of vortex W2 occurs, and it is half as large as the magnitude of the normal force. The relatively small, asymmetric boundary layer disturbance influences the separation point as well as the vortices which can migrate slowly away from the body of revolution to the side. (In contrast to this, for example, on a Delta wing, the separation point is fixed at the sharp leading edge so that it is hardly possible to change the vortex position).

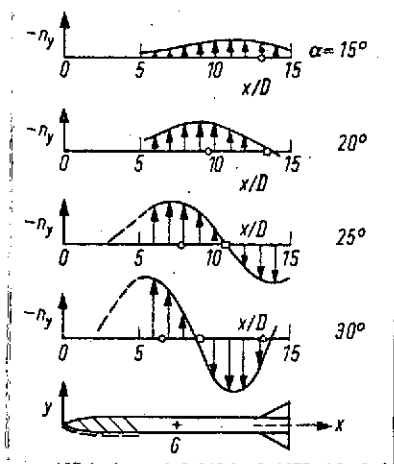


Figure 7. Side force distribution.

Shedding position of the vortices:

○	□	△
W1	W2	W3

- - - boundary layer greatly disturbed

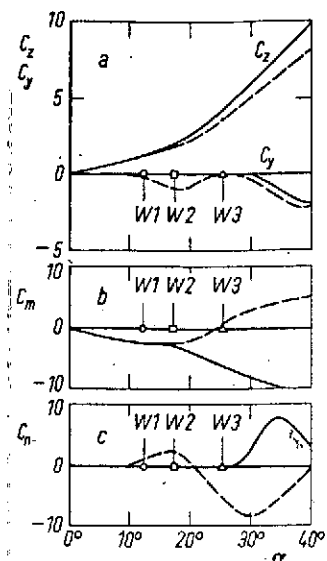


Figure 8. Forces and moments according to static measurements, Model 1 without fins.

— boundary layer not disturbed;  
- - - boundary layer disturbed

## 4.2. Bodies of revolution with fins

### 4.2.1. Forces and moments

The relationship between the  $\alpha x/D$  values for separation of the vortices and the forces and moments could also be measured with the models having fins.

Without boundary layer disturbance, the side force and the yaw moment (Figure 9) already occurred at  $\alpha > 15^\circ$  or  $\alpha x/D \approx 4.2$  when vortex asymmetry began. Without fins, the yaw moment and the normal force could only be detected when shedding of the first vortex took place at  $\alpha > 28^\circ$  and  $\alpha x/D \approx 7.3$ . The influence of the vortices which had not yet been shedded but were already asymmetric on the fins is relatively large.



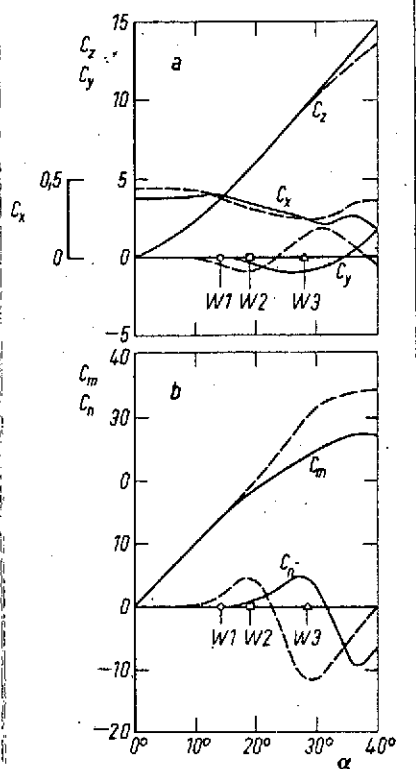


Figure 9. Forces and moments according to static measurements, Model 1 with fins.

— boundary layer not disturbed;  
 - - - boundary layer disturbed

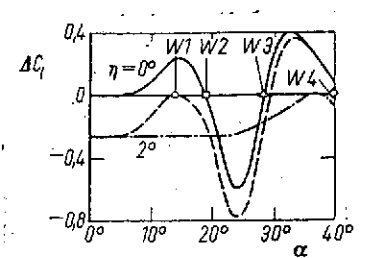


Figure 10. Roll moments, Model 1.

— fin angle  $0^\circ$ , boundary layer disturbed;  
 - - - fin angle  $2^\circ$ , boundary layer disturbed;  
 - · - fin angle  $2^\circ$ , boundary layer not disturbed

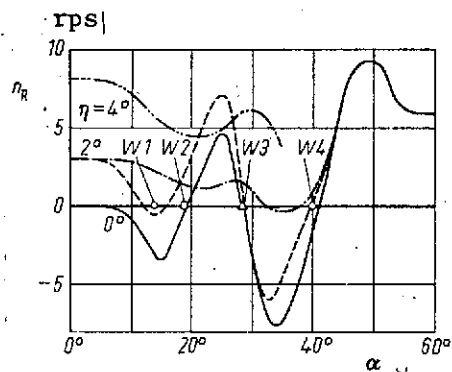


Figure 11. Rotation frequency, Model 1.

— fin angle  $0^\circ$ , boundary layer disturbed;  
 - - - fin angle  $2^\circ$ , boundary layer disturbed;  
 - · - fin angle  $2^\circ$ , boundary layer not disturbed  
 - · · - fin angle  $4^\circ$ , boundary layer not disturbed

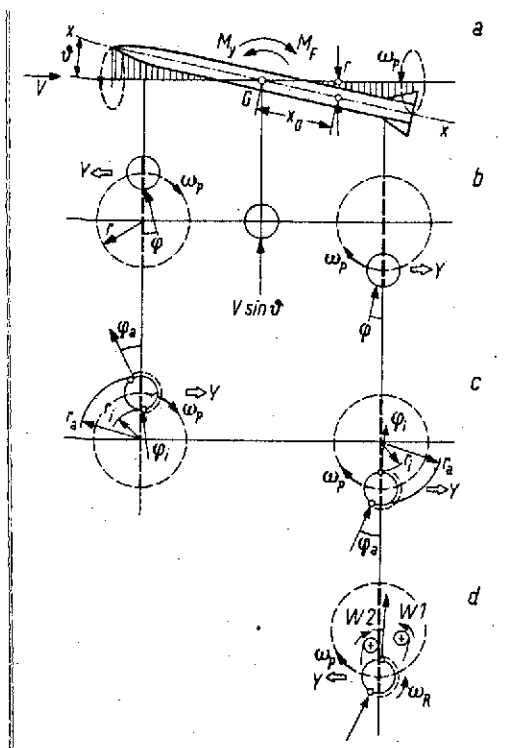


Figure 12. Fuselage flows for coning motion.

- - - coning plane which rotates at  $\omega_p$  around the wind tunnel axis

measurements. At  $\alpha > 15^\circ$ , the coefficient  $C_{l0}$  changed approximately in proportion to  $\sin 4\phi$  (see [9]).

When the boundary layer was disturbed, strong roll moments  $M_{C1}$  were superimposed on the  $C_{l0} \sim \sin 4\phi$ , which according to Figure 10 changed sign when the shedding condition was satisfied for vortices  $W1$ ,  $W2$ ,  $W3$  and  $W4$  in the flow region of the fins.

Using the same model and with free rotation around the longitudinal axis, the direction of rotation changed according

When the boundary layer is disturbed, the differences in the yaw moments with and without fins are small. With fins, the values  $[C_{l0} x/D]$  were related to  $x = 14 D$ , so that the vortex centers approximately reached the fin leading edges (Table 2). In the case of bodies with fins, the side force changes sign, which was not found without fins.

#### 4.2.2. Roll moments and rotation

Without any disturbance of the body boundary layer, the model with zero incidence fins began to rotate at  $\alpha > 40^\circ$ , when the vortices separated in an unsteady fashion from the fin leading edges. According to [5], for  $\alpha < 15^\circ$  we were not able to detect any roll moments in the static

to the  $\alpha/D$ -values (Figure 11). The autorotation and the reversal of the rotation direction are caused by a large change in the flow direction in the wake region as shown by the directional arrows in Figure 5c, as well as by directional changes of the vortex axes shown in Figure 6 (see also [9]).

The change in the direction of the roll moment was related in [6] with the shedding condition of the vortices for the Mach number  $M = 1.4$ . In this case there was a slightly bent model tip, which was the reason for vortex asymmetry (Table 2).

/287

If the fins are set at incidence of  $\eta = 2^\circ$ , then a constant roll moment as well as a constant rotation frequency is superimposed on to the curve for  $\eta = 0^\circ$ . Without any boundary layer disturbance, the influence of the vortex asymmetry is small (Figure 11). At a rotation rate of a few rotations per second, an effect is produced which is comparable to the Magnus effect. The vortices become asymmetric when they are produced at  $\alpha > 5^\circ$  and reduce the rotation rate. For  $\eta = 2^\circ$ , the rotation provided by the fins at incidence is reduced, when the first vortex is shedded at  $\alpha > 28^\circ$ . For  $\eta = 4^\circ$ , the rotation becomes so rapid that the direction of rotation is no longer reversed by the vortices. (The autorotation (Figure 11) was also filmed).

## 5. CONING MOTION

Rotationally symmetric projectiles do not cone in a preferred plane. The longitudinal axis always moves along a conical surface after the coning motion has been excited by a disturbing moment. If there is sufficient pitch moment, which is produced by sufficiently large stabilization fins, it is possible for coning angles of up to about  $10^\circ$  to occur. After this, the projectile cones back to the zero position.

Coning angles much larger than  $10^\circ$  [1, 3] were measured due to very large perturbation moments or because of coupling of the rotation and coning oscillations. The coning motion could not be presented even with very large fins [3]. This points out that the pitch moment is not as important as the yaw moment. The ISL measurements show that for coning motion, the flow processes over the body predominate over the body-stabilization fin effects.

In order to describe the processes which occur when a statically stable projectile carries out very large coning motions, we will assume that the coning angle  $\vartheta$  is constant and that the coning plane rotates at a constant coning frequency  $\omega_p$  around the trajectory tangent. With the constant incident flow velocity  $V$ , the flow will be steady around the body in the body fixed system. In each cross section plane (Figure 12b), the resulting flow is composed of the two components  $V\vartheta$  and  $r\omega_p = x_0\vartheta\omega_p$  and it forms the angle

$$\varphi = x_0 \omega_p / V, \quad (6)$$

with the rotating coning plane. This angle changes with the distance  $x_0$  from the coning center  $G$ . Upstream from  $G$  the flow comes from the right and downstream from  $G$  it comes from the left towards the body. We find an approximately screw-shape flow around the body. (In the wind tunnel experiment using Model 1 for  $\vartheta = 30^\circ$  and in  $n_p = 2$  rps at the body tip and at the body base, this angle is  $\varphi = \pm 8^\circ$ .) Because of the twisted flow plane, side forces are produced whose yaw moments attenuate the coning motion because of  $M_z \approx 0.1 M_y$ .

If the flow component  $r\omega_p$  is not referred to the body longitudinal axis as was done in Figure 12b, but to the true fuselage, then this component becomes smaller to the side of the body facing the trajectory tangent than on the side facing away.

(Figure 12c). The difference  $(r \pm R) \omega_p$  can be expressed by stating that the circumferential angle between the separation line along the incident flow side and the convergent line on the wake side is larger on one side by

$$\Delta\varphi = \varphi_a - \varphi_i = D \omega_p / V. \quad (7)$$

It is remarkable that both upstream and downstream of G, it is always the same side. In Figure 12c, this is the right side. (In the wind tunnel experiment with  $\vartheta = 30^\circ$  and  $n_p = 2$  rps we find  $\Delta\varphi = 12^\circ$ ).

In addition to the screw shape flow around the body according to Equation (6) and the flow asymmetry according to Equation (7), during coning motion we also have inertia forces (for example  $\vartheta = 30^\circ$  and  $n_p = 2$  rps, the radial acceleration  $r \omega_p^2$  at the model tip is 3.5 times as large as the acceleration of gravity). It can be assumed that the centrifugal and Coriolis forces influence the flow near the wall as well as the wake flow with the asymmetric vortices. These superpositions would have to be investigated by detailed tests.

The vortex asymmetry is related with the asymmetric pressure distribution. Side forces are produced which brake the coning motion upstream of G. Downstream of G they support the coning motion (Figure 12d). The yaw moment which supports the coning motion is intensified because the vortex circulation increases with distance  $x$  from the body tip (Section 4.1.1.) The exciting side forces downstream of G become greater than the braking side forces upstream of G.

The measurement results show that the yaw moment decreases again with increasing coning angle and changes sign at a defined value of  $\varphi_{x/D}$ . This is also true in static tests with boundary layer disturbance. When this zero crossing of the yaw moment occurs, the coning motion is transformed into the steady state and the coning angle as well as the coning frequency remain constant.

In addition to the yaw moment, in the final state it is necessary for the stabilizing pitch moment  $M_y$  to also vanish. This  $M_y$  is countered by the destabilizing centripetal force moment  $M_F$ :

$$-M_F = -J \omega_p^2 \frac{1}{2} \sin 2\vartheta \quad (8)$$

In Equation (8) the transverse moment of inertia  $J$  is referred to the body center of gravity  $G$ . When

$$M_y(\vartheta) = -M_F(\vartheta)$$

then the final angle  $\varphi_E = \text{const}$  is determined by the value of  $\varphi_{x/D}$  with the yaw moment  $M_2 = 0$ .

If the body longitudinal axis moves on a conical surface in a certain direction around the trajectory tangent, then the flow asymmetry with respect to the coning plane is uniquely determined. The asymmetric vortices cannot sporadically take on a position which is the mirror image with respect to the coning plane, which is possible in the steady experiment. In addition, unique asymmetric conditions are produced by disturbing the boundary layer on one side and by rotation around the longitudinal axis. When the direction of rotation is specified, the coning plane rotates in the opposite direction around the trajectory tangent (Figure 5a).

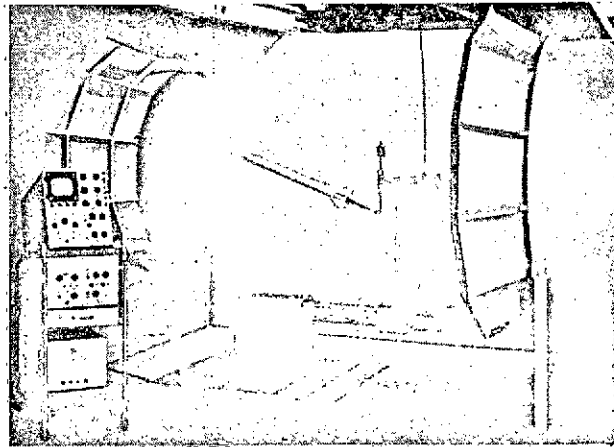


Figure 13. Test installation for coning motion with the crank arm. The crank with the model is driven by the electrical motor; balance with strain gauges on the model

### 5.1. Forces and moments

In order to measure the forces and moments during coning motion, the model was installed on a stiff crank (Figure 13). The body longitudinal axis makes an angle  $\varphi$  with the crank axis, and it was changed in steps. The moment reference point G, at a distance of  $x_G = L/2$  from the tail, was located at the intersection between the body longitudinal axis and the crank axis, which also corresponded to the wind tunnel axis. The balance with strain gauges was installed in the model. The model was driven by a small electrical motor at constant  $\varphi$  and a coning frequency of  $n_p = 1$  and 2 rps around the crank axis.

The normal forces and pitch moments during coning motion are not substantially different from those during the static measurements. The variations for the side forces and pitch moments during coning motion with Model 1 without fins (Figure 14) and with the model with zero incidence fins (Figure 15) were similar to what was found during the static measurements. The

extreme values and zero crossings of the yaw moments were located between those of the static measurements with and without boundary layer disturbance. In the model without fins as well as in the model with fins, the yaw moment changes sign at about the same coning angle. As the coning frequency is increased, this coning angle became smaller, because apparently the shedding locations of the vortices were displaced toward the tip of the model.

## 5.2. Rotation and coning motion

In these experiments, the Model 1 with zero incidence fins was installed on the driven crank and could freely rotate around the longitudinal axis. According to Figure 16, the rotation started at crank angles of  $\theta > 5^\circ$ . They reached an extreme value and changed direction, which was also the case during the steady measurements with boundary layer disturbance according to Figure 9. For coning motion, zero rotation means that, for example, one of the fins always points in the direction of the wind tunnel axis. This is called "moon motion" [2].

When the drive motor was uncoupled at the coning angle  $\theta = 24^\circ$  at the rotation frequency  $\overline{n_R} = 0$ , the crank arm continued to turn with the model because the yaw moment only changes sign at  $\theta = 30^\circ$  (Figure 15). The steady state of the coning motion is therefore not directly related to the "moon motion" because the yaw moment depends on the position of the moment reference point and the final angle is determined by the shedding state of the vortices.

The coincidence of "moon motion" and beginning excitation, called roll lock-in [2], is therefore not related with our measurements, because the coning angles were very small in those experiments and the body vortices probably played a subordinate role. In the measurements given in Figure 17, the crank arm



with a model could freely rotate around the crank axis. In addition, because of the fins at incidence, the model could rotate around the longitudinal axis. The coning motion started at  $\vartheta > 15^\circ$ , exceeded an extreme value and changed the coning direction at the same angle at which the yaw moment changed its sign (Figure 15). As the rotation rate was increased, the coning angle  $\vartheta_E$  became smaller for  $n_P = 0$ .

Since all of the curves for coning motion are very similar to the curves found during the static measurements with boundary layer disturbance, we give the suspected shedding values for the vortices in Figures 14, 15, 17 as well as in Table 2. The similar behavior of the vortices was confirmed by comparing the streamlines near the wall. The boundary layer pictures were similar at corresponding values of  $\alpha x/D$  and  $\vartheta x/D$  [9].

### 5.3. Free coning motion

According to Figure 18, the model could cone around a transverse wire, which passed through the model center of gravity and had a small influence on the flow around the body. In addition, a Cardan joint was installed in the body so that the model could cone at coning angles  $\vartheta < 45^\circ$  in all directions around the wind tunnel axis around its fixed center of gravity. Except for the short center part containing the Cardan joint, the front and the back part of the Model 7 could rotate together around the model longitudinal axis. Since we were not successful in starting the coning motion when the model was only deflected in a coning plane, we had to install an additional drive crank. The crank pin was introduced into a central hole in the model tail. The model axis was driven by an electrical motor and it was rotated around a conical surface at the coning angle  $\vartheta_K$  around the wind tunnel axis. The crank pin could be pulled out of the tail hole

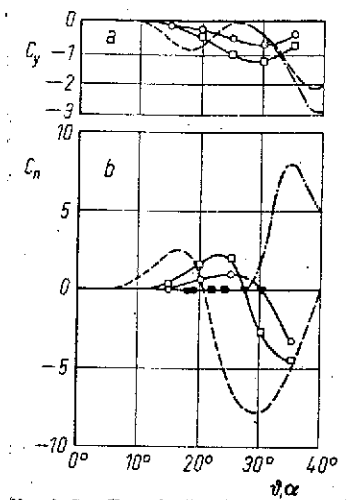


Figure 14. Side force and yaw moment, Model 1, without fins.

— crank driven by

	$n_p$ rps
○	1
□	2

- - - static measurement with disturbance of the boundary layer;

- . - static measurement without disturbing the boundary layer;

Shedding position of vortices:

●	■	▼
W 1	W 2	W 3

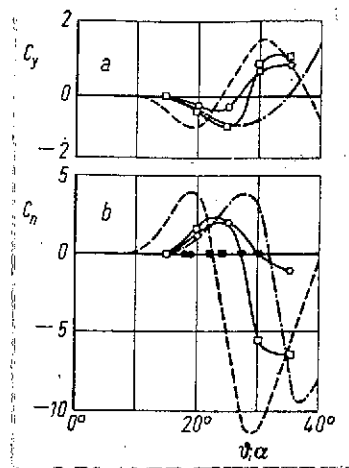


Figure 15. Side force and yaw moment, Model 1, with fins, nose rotates.

— crank driven at

	$n_p$ rps
○	1
□	2

- - - static measurement when disturbing the boundary layer;

- . - static measurement without disturbing the boundary layer;

Shedding position of vortices:

●	■	▼
W 1	W 2	W 3

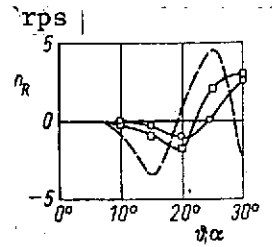


Figure 16. Autorotation, Model 1 rotates freely around the longitudinal body axis, fins not at incidence.

crank driven by

	$n_p$ rps
○	1
□	2

-- static measurement with disturbance of boundary layer

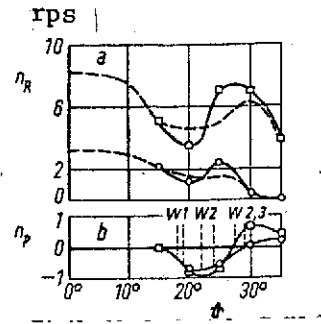


Figure 17. Rotation and coning motion, Model 1 rotates freely around body longitudinal axis, crank and model rotate without motor drive at a frequency of  $n_p$  around the wind tunnel axis.

	Fin angle[°]
○	2
□	4

-- rotation without coning motion  $n_R(a)$

while in the wind tunnel air stream so that the model could continue to cone without any external drive.

For a fin setting of  $\eta = 4^\circ$ , the Model 7 was driven by the crank at  $n_p = 1$  rps. In order for the coning motion to begin, it was necessary to select the crank angle  $\theta_K \geq 19^\circ$ , because only at this angle does the first vortex shed. After the crank pin was pulled out of the tail hole at time  $t = 0$ , the cone angle increased (Figure 19) and reached a final value  $\theta_E = 30^\circ$ , which fluctuated around  $\pm 1^\circ$ . According to the measurements shown in Figure 17, the rotation frequency increased from  $n_R = 3.5$  rps to 7.5 rps. The coning frequency remained constant at  $n_p = 1.01$  rps (Curve A in Figure 19).

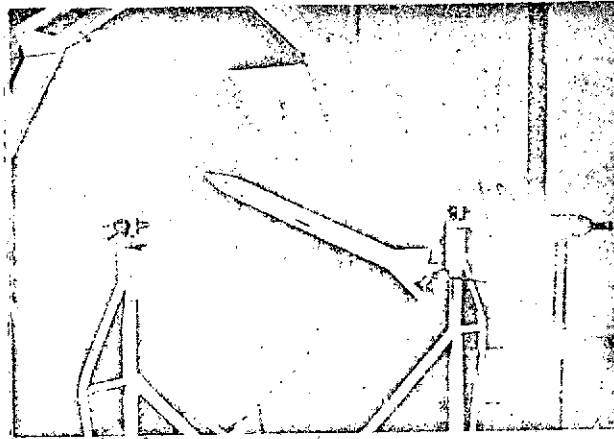


Figure 18. Test installation for coning motion around fixed center of gravity. Cardan joint in the center of the model. The front and back part of the model rotate together around the body longitudinal axis. Build-up of the coning motion by the crank, and the crank pin is pulled out of a central hole in the model tail during the test.

For  $\vartheta_K < 19^\circ$  it was only possible to introduce coning motion when  $n_p$  was increased. For example, at  $\vartheta_K = 12^\circ$  it was necessary to make  $n_p \geq 2.2$  rps, in order to provide a larger centeripetal force moment and the cone angle  $\vartheta \geq 19^\circ$  (Curve B in Figure 19).

The same final angle  $\vartheta_E = 30^\circ$  was obtained with Model 1 with about the same moment of inertia according to Table 1 and Figure 20, at which only the tail could freely rotate without the fins at incidence. (Referred to the rotating coning plane, the motion of the "non-rotating" remaining fuselage corresponds to the rotation  $n_H = -n_p$ ). The other models with various moments of inertia and various degrees of slenderness also coned to a final angle, which corresponded to the value of  $|\vartheta L/D|$  for the equalized yaw moment. The statically stable Model 6 without fins also reached a final state, corresponding to the yaw moment measurements given in Figure 14.

The suspected shedding values  $|\vartheta L/D_m|$  for the beginning of excitation and  $|\vartheta L/D_{w2.3}|$  for the final state are shown in Figure 20 as curves (Table 2). The measured values correspond to these curves.

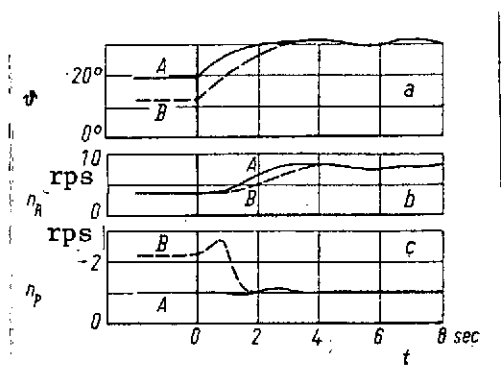


Figure 19. Transient oscillation process of coning motion according to Figure 18, Model 7, fin angle  $4^\circ$ .

$t = 0$ : pulling out of the crank pin from the tail hole

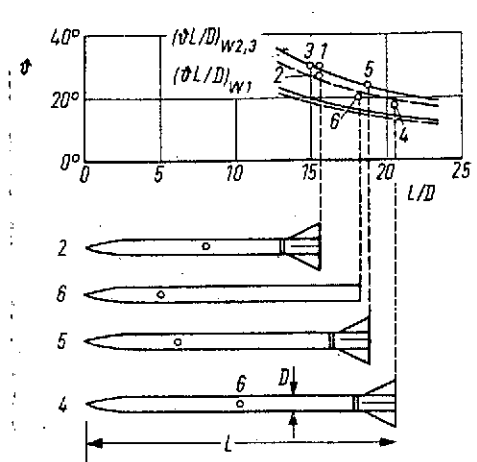


Figure 20. Slenderness ratio  $L/D$  and coning motion angle  $\vartheta$ , Models 1 to 6 according to Table 1, tail rotates, fins not at incidence.

$(\vartheta L/D)_{W1}$  initial value;  $(\vartheta L/D)_{W2,3}$  adjusted state

	$n_p$ [rps]
—	1
- - - -	2

For Models 4 and 6, the values of  $\vartheta_E$  are below the curve for  $n_p = 1$  rps, because here the coning frequency was even smaller (Table 1).

In addition, in all the measurements we reduced the flow velocity from 34.2 m/sec to 20.4 m/sec. The final angles  $\vartheta_E$  remained the same and the coning frequency coefficient  $D \omega_p / \sqrt{V}$  remained constant [9].

In Figure 21 we show the measured final angles and the angles calculated according to Equation (8). The measured static pitch moments  $M_y$  according to Table 1 were substituted. The

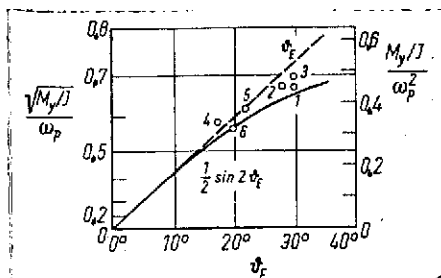


Figure 21. Final angle  $\phi_E$  and coning frequency  $\omega_p$  according to Equation (8)

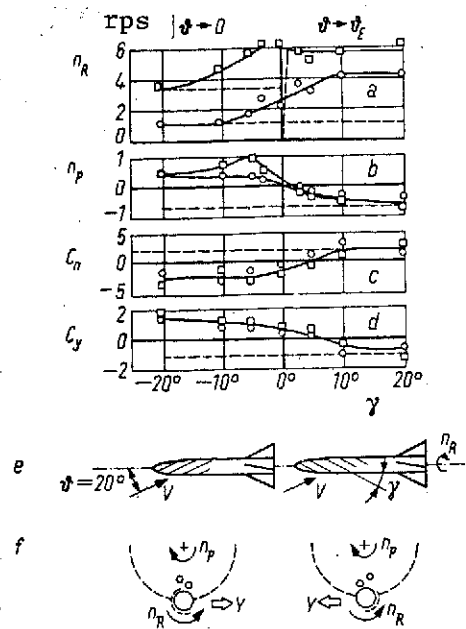


Figure 22. Boundary layer disturbance varies, 8 disturbing bands 5 mm x 0.25 mm, crank angle 20°.

	Fin angle [°]
○	2
□	4

--- without disturbing the boundary layer

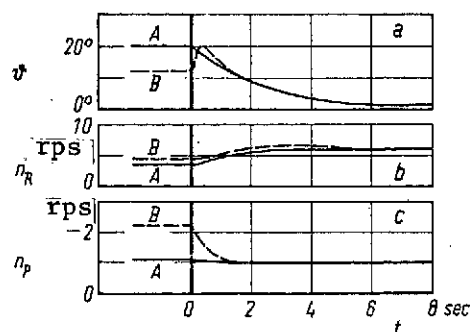


Figure 23. Damping of the coning motion. Fin angle 4°, inclination angle of the disturbing elements - 5°

agreement is satisfactory.

#### 5.4. Prevention of Coning motion

Coning motion could only be prevented when the asymmetry of the vortices intensified by rotation was opposed by the asymmetry caused by boundary layer disturbance. The rotation caused by fins at incidence had to be fast enough so that the changing vortex asymmetry could not reverse the direction of rotation (Figure 17).

The inclination angle of the disturbing elements used for asymmetric disturbance of the boundary layer was  $\gamma = 45^\circ$  and the measured results are given in Figures 5 - 11. For the example of the measurement given in Figure 22, the inclination angle  $\gamma$  was changed in steps and the crank angle of the measurement arrangement was maintained constant at  $\theta = 20^\circ$  in Figure 13.

The rotation frequency in Figure 22 increased with increasing  $\gamma$  above the value obtained in Figure 17 without the disturbance.

The direction of coning motion in Figure 22b for negative  $\gamma$  was opposite to the coning motion without disturbance elements which also applies for the side forces and yaw moments shown in Figures 22 c and d.

By properly selecting the inclination angle of the disturbing elements, it is possible to compensate for the yaw moments. This was the case when  $\gamma = -5^\circ$  and therefore when screw inclination angles of the flow near the wall were selected counter to the direction of rotation. When the model was moved around the wind tunnel axis using the same configuration as in Figure 18 and the same initial conditions as in Figure 19, then according to Figure 23,

the coning angle  $\theta \geq 19^\circ$  was reached but the coning angle did not occur. It did not occur even when the crank frequency was greatly increased. The model coned back to the zero position in all cases.

The prevention of coning motion according to Figure 23 and the coning motion according to Figure 19 were filmed.

## 6. SUMMARY

Experiments in a subsonic wind tunnel showed that coning motion of slender bodies of revolution with and without stabilization fins can be related to the behavior of the vortices which are shedded asymmetrically along the wake side of the body. As a criterion for the shedding of the vortices we found the distances  $x/D$  from the body tip at which the vortex axes have a clear break. After this point, these axes leave the body fixed wake region. The product of the distance  $x/D$  and the angle of attack  $\alpha$ , or the cone angle  $\theta$  was constant for the shedding point of each vortex.

The difference in the  $\alpha x/D$  values in static measurements with asymmetric boundary layer disturbance agreed approximately with the separations of the vortices which separate periodically in time from circular cylinders in an oblique flow.

The  $\alpha x/D$  values of the static measurements without boundary layer disturbances were considerably larger than the  $\theta x/D$  values for coning motion. The vortices became asymmetric at  $\alpha x/D = 4.2$  and the first vortex was shedded at  $\alpha x/D = 7.3$ . During coning motion, the vortex became asymmetric as it was produced at  $\theta > 5^\circ$ .



1. At the beginning of coning motion it was necessary, for the body longitudinal axis to move along a conical surface and for the first vortex to be shedded at the fuselage tail or in the flow field of the fins, respectively. It was also necessary that  $4.7 \leq \theta L/D \leq 5.0$ .

2. The final coning motion state with  $\theta = \text{const}$  and  $\omega_P = \text{const}$  occurred at  $7.1 \leq \theta L/D \leq 7.8$ . At this point, the first and second vortices had already been shedded and the third vortex had already formed.

3. The autorotation of the body with the fins at zero incidence started during coning motion as the vortices became asymmetric. The direction of rotation was reversed each time when the second, third and fourth vortices were shedded. When the body was already rotating because of the fins set at incidence, the rotation was disturbed by the shedded vortices.

4. The  $\theta x/D$  values become smaller with increasing coning frequency and with increasing rotation frequency, because the vortex shedding in these cases is supported.

5. When disturbing elements were installed on the surface of the body in the shape of screws during the static measurements, the vortices, the side forces and the yaw moments varied in a way similar to what occurred during coning motion.

6. If the fins were inclined so much that the rotation direction would no longer reverse because of the vortex shedding, then the direction of rotation of coning motion was always opposed to the direction of rotation. It was only in this case that we were successful in preventing the coning motion by selecting the inclination angle of the disturbing elements

in a direction opposite to the inclination angle of the flow near the wall caused by the rotation.

The experimental investigations in [3, 4, 6] lead one to suspect that for supersonic velocities, it will be possible to establish a connection between the vortex shedding and the coning motion.

#### REFERENCES

1. Chadwick, W. R. The Flight of a Bomb with Cruciform Tail. In: The Fluid Dynamics Aspects of Ballistics. AGARD CP Vol. 10, 1966, pp. 319-339.
2. Nicolaides, J. D. A Review of Some Recent Progress in Understanding Catastrophic Yaw. AGARD Rep.551, 1966.
3. Curry, W. H. and J. C. Uselton. Some Comments on the Aerodynamic Characteristics of the "Tomahawk" Sounding Rocket. Sandia Corp., N.M./U.S. SCR, 66/997, 1967.
4. Tobak, M., L. B. Schiff and V. L. Peterson. Aerodynamics of Bodies of Revolution in Coning Motion. AIAA Journ. Vol. 7, 1969, pp. 95-99.
5. Fiechter, M. Projectile with 4 Triangular Fins without Roll Moment. ISL, Technical Communication T 28/64, 1964.
6. Thomson, K. D. and D. F. Morrison. On the Asymmetric Shedding of Vortices from Slender Bodies at Large Angles of Yaw. Weapons Research Establishment, Salisbury, South Australia, Techn. Note HSA 106, 1965.
7. Fiechter, M. Vortex Systems of Slender Bodies of Revolution. Yearbook 1969 of the DGLR, pp. 77-85.
8. Grosche, F.-R. Wind Tunnel Investigations of the Vortex System over a Slender Body of Revolution at Incidence With and Without Wings. Z. Flugwiss, Vol. 18, 1970, pp. 208-217.

9. Fiechter, M. Coning Motion and Autorotation of Slender Projectiles. ISL Report in preparation.
10. Sarpkaya, T. Separated Flow about Lifting Bodies and Impulsive Flow about Cylinders. AIAA Paper 65-395, 1965.

Translated for National Aeronautics and Space Administration under contract No. NASw 2483, by SCITRAN, P. O. Box 5456, Santa Barbara, California 93108.